Article

Stepwise Monomicelle Assembly for Highly Ordered Mesoporous TiO₂ Membranes with Precisely Tailored Mesophase and Porosity

Kun Lan,* Lu Liu, Jiayu Yu, Yuzhu Ma, Jun-Ye Zhang, Zirui Lv, Sixing Yin, Qiulong Wei,* and Dongyuan Zhao*

Read Online

ACCESS | 📊 Metrics & More | 📰 Article Recommendations | 🆂🅸 Supporting Information

ABSTRACT: Mesoporous materials with crystalline frameworks have been acknowledged as very attractive materials in various applications. Nevertheless, due to the cracking issue during crystallization and incompatible hydrolysis and assembly, the precise control for crystalline mesoscale membranes is quite infertile. Herein, we presented an ingenious stepwise monomicelle assembly route for the syntheses of highly ordered mesoporous crystalline TiO₂ membranes with delicately controlled mesophase, mesoporosity, and thickness. Such a process involves the preparation of monomicelle hydrogels and follows self-assembly by stepwise solvent evaporation, which enables the sensitive hydrolysis of TiO₂ oligomers and dilatory micelle assembly to be united. In consequence, the fabricated mesoporous TiO₂ membranes exhibit a broad flexibility, including tunable ordered mesophases (worm-like, hexagonal *p6mm* to body-centered cubic *Im3̄m*), controlled mesopore sizes (3.0−8.0 nm), and anatase grain sizes (2.3−8.4 nm). Besides, such mesostructured crystalline TiO₂ membranes can be extended to diverse substrates (Ti, Ag, Si, FTO) with tailored thickness. The great mesoporosity of the *in situ* fabricated mesoscopic membranes also affords excellent pseudocapacitive behavior for sodium ion storage. This study underscores a novel pathway for balancing the interaction of precursors and micelles, which could have implications for synthesizing crystalline mesostructures in higher controllability.

KEYWORDS: mesoporous materials, self-assembly, thin films/membranes, titanium dioxide, energy storage
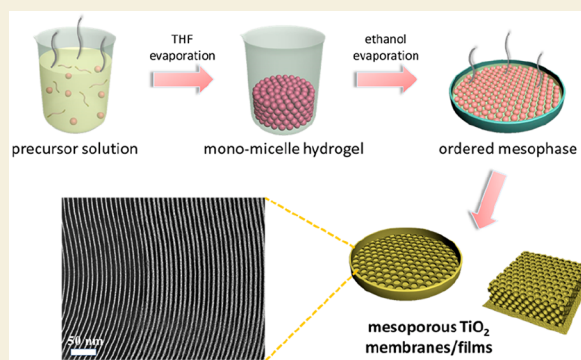
INTRODUCTION

Crystalline mesoporous materials have emerged in the past decades due to their fascinating mesoporosity and crystallinity, which promise various applications ranging from optoelectronic, energy storage, and conversion devices.[1−6] Although crystalline mesostructures are usually constrained to their incompatibility between fast hydrolysis of precursors and moderate self-assembly of micelles, it was first demonstrated in 1995 when Antonelli showed that a ligand could retard fast hydrolysis of metal sources and form a reduced size as assembly units for an ordered TiO₂ mesostructure.[7] Certain strategies (*e.g.*, sol−gel method, hydrothermal process, evaporation method) have been developed for creating well-defined crystalline mesoporous metals,[8−11] oxides,[12−14] and other compounds.[15−19] Unfortunately, the construction of crystalline mesoporous membranes/films currently remains a great challenge, and the precision control of mesoscale architectures, porous configurations, and mesoscopic parameters also remains far out of reach.[5,20] In this regard, the development or optimization of reliable strategies and comprehending of assembly chemistries of mesostructured crystalline membranes are quite imperative.

Unlike SiO₂, molding crystalline mesostructured membranes (CMMs), such as TiO₂, remains quite challenging. First, the crystallization at high temperature unavoidably leads to the segregation and shrinkage of as-prepared membranes due to the vanishing of interaction with substrates. Although some strategies have been developed to suppress film cracking and increase thickness,[21−23] the film continuity and integrity still remain unsettled for crystalline membranes. Second, the undesired control is majorly ascribed to the fundamental issues in crystalline mesostructures: fast hydrolysis of metal precursors, weak interaction of precursors and surfactants, and mesostructural collapse during crystallization.[24−26] In response to these restrictions, the employment of specific metal precursors[27] and surfactants,[8,28] ligands, or chelates[12,29,30] have been used in order to maintain a moderate and stable self-assembly procedure. Consequently, these fundamental princi-

ples severely restrict the accessibility and tunability of CMMs, resulting in less success compared to amorphous mesoporous silica and carbon. One of the key limitations is the insufficient controllability and scanty versatility of CMMs due to the narrow range of micelle assembly for hyperactive metal precursors. Taking the representative evaporation-induced self-assembly (EISA) approach[31] as an example, a dilute precursor solution is generally required to balance hydrolysis, leading to mesoporous films with a finite thickness and a stationary mesophase. Alternatively, the hard-templating method[32−34] is, currently, a reliable pathway for generating reverse mesostructures in spite of its complicacy, but such replication is unsuited to delicate membranes/films. So far, although certain CMMs have been synthesized,[35−37] it still remains difficult to realize accurate control over the self-assembly process with satisfied tunability. The tardy progress mainly arises from the lack of understanding over the micellar self-assembly on a subnanometer scale, including congruous precursor hydrolysis, insufficient template interaction, as well as crystallization on substrates. Explorations on promoting the endurance and stability of metal precursors would enable access to the desired manipulation over mesoporous membranes in crystalline networks.

Herein, we present a stepwise monomicelle assembly method to construct highly ordered mesoporous crystalline TiO$_2$ membranes with a precisely tailored mesophase, porosity, and thickness. Through first obtaining a monomicelle hydrogel from pre-evaporation and subsequent self-assembly from second-evaporation, we are able to carefully monitor the sensitive hydrolysis of TiO$_2$ oligomers and dilatory micelle assembly, respectively. The intermediate monomicelle hydrogels during the first evaporation can be retained stably and afford sufficient time for slow titanium hydrolysis, which allows the ingenious separation of precursor hydrolysis and surfactant−source interaction without apprehending interactive variations. Besides, during crystallization under an inert atmosphere, the residual carbon in frameworks prohibits excessive TiO$_2$ grain growth and provides a strong adhesion to substrates, which guarantees the membrane integrity. As a result, the formed mesoporous TiO$_2$ membranes with a well-crystalline scaffold possess a uniform and continuous membrane morphology without obvious segregation. The fabricated mesoporous TiO$_2$ membranes exhibit a saltant flexibility, including tunable ordered mesophases (from disordered to hexagonal to cubic), controlled mesopore sizes (3.0−8.0 nm) and grain sizes (2.3−8.4 nm), as well as varied thickness (from ∼280 nm to ∼2 μm). Such stepwise control allows for a broader reactive region with a high precursor concentration and sufficient assembly time. Furthermore, the good expansion of the mesostructured TiO$_2$ membranes to various substrates is demonstrated, followed by the techno-logical potential of such mesoscopic membranes for high-performance pseudocapacitive sodium storage. A capacity retention of 65% over 20,000 cycles (10 A g^{-1}) and an ultrafast kinetics from pseudocapacitance at a sweep rate of 100 mV s^{-1} have been achieved, demonstrating a blueprint to advanced energy storage capable of fast sodium ion uptake.

■ EXPERIMENTAL SECTION

Materials

Pluronic triblock copolymer poly(propylene oxide)-*block*-poly-(ethylene oxide)-*block*-poly(propylene oxide) (F127, Mw = 12600, EO$_{106}$PO$_{70}$EO$_{106}$) was purchased from Acros Corp. Tetrabutyl titanate (TBOT, 99.5%) was purchased from Sigma-Aldrich Corp. Tetrahydrofuran (THF), hydrochloric acid (HCl, 36−38 wt %), acetic acid, and anhydrous ethanol were purchased from Sinopharm Chemical Reagent Co., Ltd. (China). All reagents were purchased from commercial sources and used without further purification.

Preparation of PEO-*b*-PPO-*b*-PEO/TiO$_2$ Oligomer Composite Monomicelle Hydrogels

The monomicelle composite hydrogels were synthesized according to the approach of refs 32 and 38. For a typical synthesis, 1.5 g of triblock copolymer Pluronic F127 was added into 30 mL of THF, which was followed by adding 2.4 mL of acetic acid as a chelating agent and 3.2 mL of concentrated HCl as a stabilizer to retard fast hydrolysis of the titanium precursor. After stirring for 5 min to form a transparent solution, 3.4 g of TBOT was quickly added into the mixture. After stirring for another 5 min, the golden yellow solution (around 40 mL in total) was transferred into two volumetric flasks (30 mm × 50 mm) and kept in an oven at 45 °C for 24 h to preferentially evaporate THF. Notably, the relative humidity was kept at less than ∼45% for preventing excessive hydrolysis into unassembled TiO$_2$ nanoparticulates; otherwise, a crimson precursor solution was formed. The white yellow hydrogels comprised of PEO-*b*-PPO-*b*-PEO/TiO$_2$ oligomer composite monomicelles were obtained and stored in a drying box in order to decrease exposure in air.

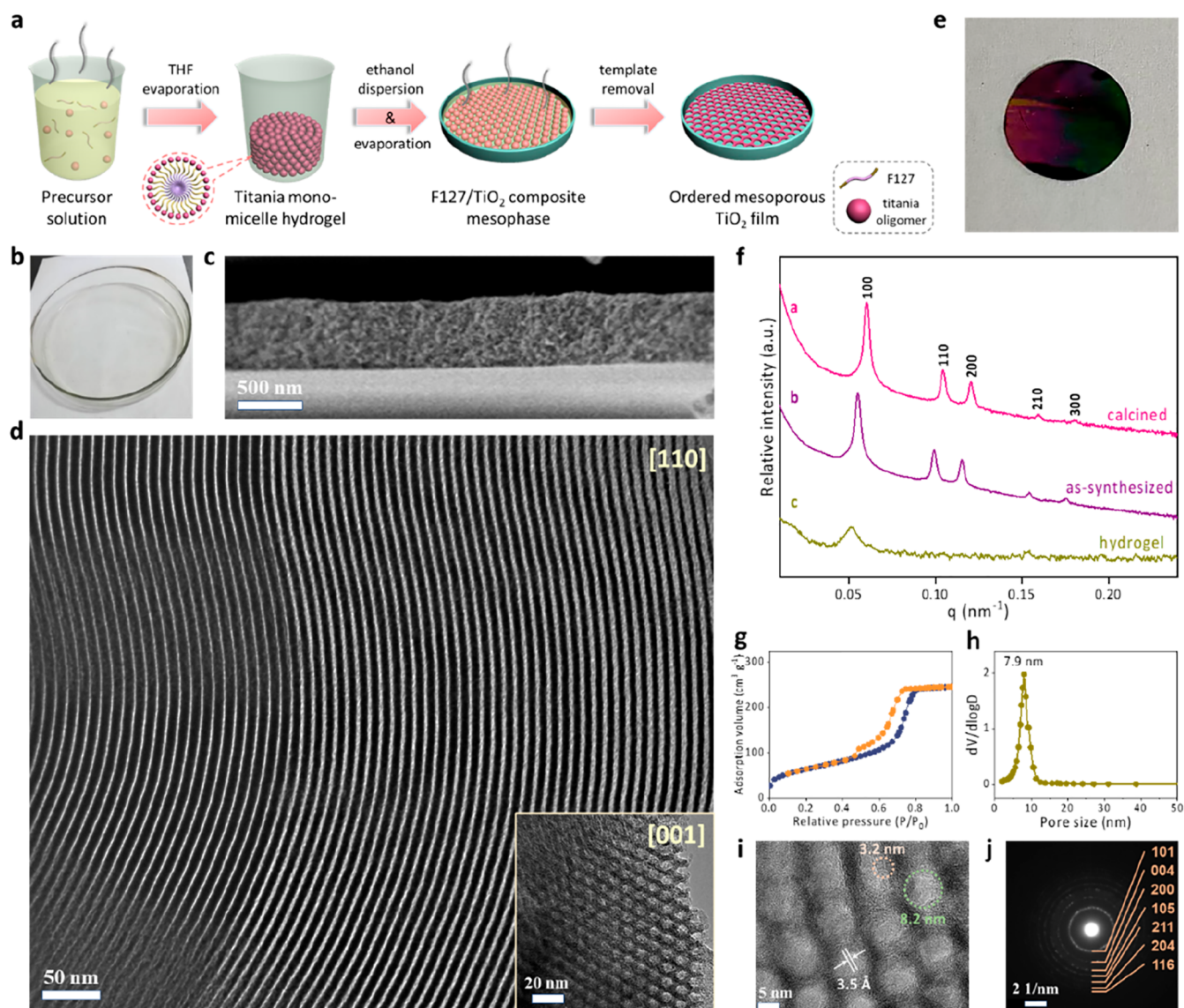### Synthesis of Ordered Mesoporous TiO$_2$ Membranes on Substrates

The ordered mesoporous TiO$_2$ membranes were fabricated through a stepwise monomicelle self-assembly process. For a typical synthesis of the hexagonally mesoporous membranes, the prepared monomicelle hydrogel (around 5.0 g) was dispersed into 25 mL of anhydrous ethanol, and the resultant mixture was stirred for 10 min, forming a transparent solution. Next, 5.0 mL of the monomicelle dispersion (0.06 g/mL) was poured into an open Petri dish (∼20 cm in diameter) and transferred into an oven at 45 °C for 24 h. After the transparent sol was gelled, the resultant gel was dried at 80 °C for 6 h in an oven to form inorganic−polymer hybrids. The mesoporous TiO$_2$ membranes were finally obtained after the calcination in nitrogen for 3 h with a slow heating rate of 1 °C min^{-1}. The samples annealed at 350, 400, 450, 500, 550, and 600 °C were denoted as meso-TiO$_2$-X (where X represents the annealing temperature). Additionally, detailed synthetic conditions for the meso-TiO$_2$ membranes in different substrates and thicknesses were summarized in Table S1.

Electrochemical Measurements

The electrodes were prepared by *in situ* growth of the mesoporous TiO$_2$ membranes on Ti foil as the active materials without any conducting additives or binders. Before measurements, the *in situ* prepared membranes were annealed under nitrogen at 500 °C for 3 h, and the thick Ti foils (0.1 cm) were used in order to prevent curling up during calcination. 2032-Type coin cells, by using TiO$_2$ materials as a working electrode, a sodium foil as counter and reference, and a glass fiber separator (Whatman, GF/A) saturated with 1.0 M NaPF$_6$ in diethylene glycol dimethyl ether as electrolyte, were assembled in argon-filled glove boxes. All the electrochemical tests were undertaken on an electrochemical workstation (Bio-Logic VMP3) at room temperature. Discharge−charge tests for TiO$_2$ electrodes were carried out with a duration time of 0.6 h and a rest time of another 0.5 h for each step (0.2 to 500 mV s^{-1} in 0.01−2 V vs. Na$^+$/Na).

Material Characterizations

Optical photographs were taken with a Canon digital camera. The morphology and structure of samples were observed by field-emission scanning electron microscopy (FESEM, Hitachi Model S-4800). Nanostructures of samples were observed by transmission electron microscopy (TEM, JEM-2100F). Mesophases of samples were measured by small-angle X-ray scattering (SAXS, Nanostar U) using Cu Kα radiation at 40 kV with an incident angle at 0.02°. Crystal phases of samples were identified by wide-angle X-ray diffraction

Figure 1. Synthesis and characterization of the highly ordered mesoporous TiO₂ membranes. (a) Schematic of the formation process for the ordered mesoporous TiO₂ membranes from stepwise monomicelle assembly. (b) Photonic graph of the as-prepared mesostructured TiO₂ membrane on glass. (c) Cross-sectional SEM image and (d) TEM images of the ordered mesoporous TiO₂ membranes taken along the [110] and (Inset) [001] incidence. (e) Photonic graph of the mesoporous TiO₂ membranes on Ti foil. (f) SAXS patterns of the ordered mesoporous TiO₂ membrane, as-synthesized membrane before annealing, and titania monomicelle hydrogel. (g) The nitrogen sorption isotherms and (h) pore size distribution curve, (i) HRTEM image, and (j) corresponding SAED pattern of the ordered mesoporous TiO₂ membranes after calcination in nitrogen at 400 °C.

(WAXRD, Bruker D8) using Cu Kα radiation (40 kV, 40 mA) and a Raman spectrometer (LabRamFR, Horiba) on an Ar⁺ laser at an excitation wavelength of 514.5 nm. The surface area and pore size distribution of samples were measured by nitrogen sorption isotherms (Micromeritics Tristar 3020) at 77 K. The Brunauer−Emmett−Teller (BET) method was utilized to calculate surface areas, and the Barrett−Joyner−Halenda (BJH) model was used to calculate pore size distributions.

RESULTS

Stepwise Monomicelle Assembly

The highly ordered mesoporous titania membranes with well-crystalline frameworks could be fabricated through a stepwise monomicelle assembly process (Figure 1a, Figure S1). To be specific, acidic THF/H₂O solution containing amphiphilic triblock copolymer Pluronic poly(ethylene oxide)-*block*-poly-(propylene oxide)-*block*-poly(ethylene oxide (PEO-*b*-PPO-*b*-PEO) and a titanium source was employed and evaporated under a low temperature (45 °C). A water-rich hydrogel that involved stably retained F127/TiO₂ monomicelle subunits (∼6.9 nm in diameter) was obtained after preferential THF evaporation due to its lower boiling point (66 °C) (Figure S2). During this step, the fast hydrolysis could be finely retarded and the preformation of the monomicelle subunits allowed for great tunability since there were no limitations caused by excessive aggregation (TiO₂−TiO₂) and undesired interaction (TiO₂−micelle) in the subsequent assembly. The second step involved a followed EISA process of ethanolic dispersion of monomicelles with adjustable concentration and time, which enabled production of the ordered mesostructured TiO₂
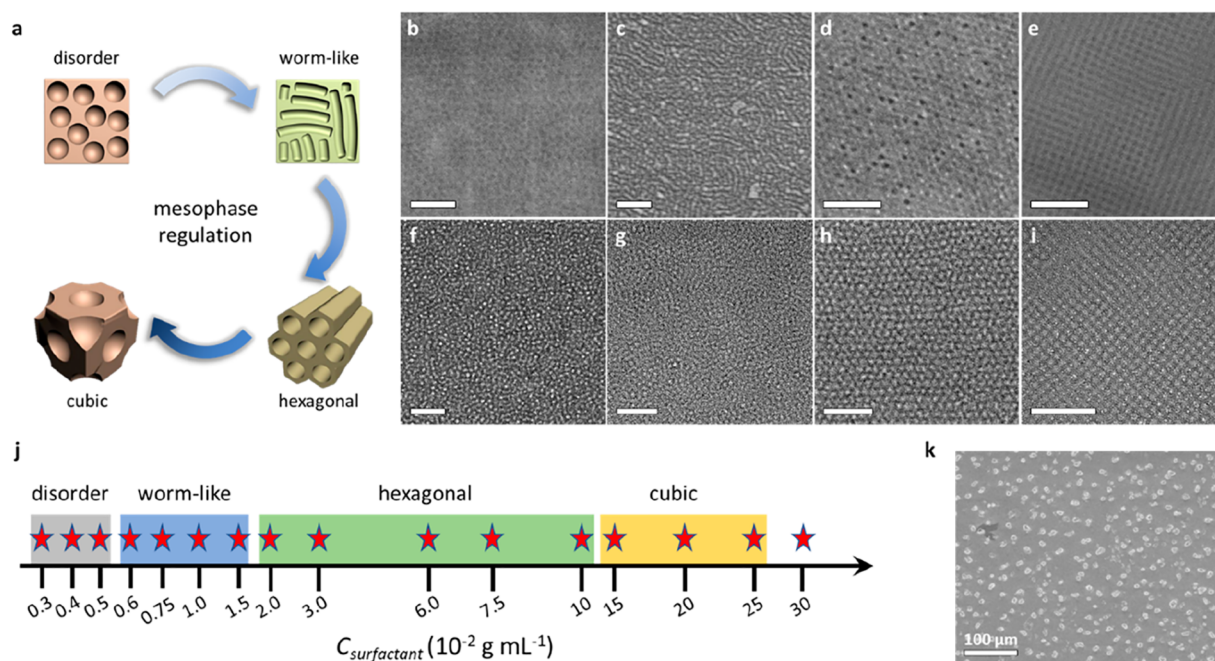
Figure 2. Accurate TiO$_2$ mesostructural regulation. (a) Schematic of the mesostructured revolution of the mesoporous TiO$_2$ membranes from disordered to cubic mesophase with the increase of surfactant concentration. (b−i) Representative FESEM images and corresponding TEM images of the varied TiO$_2$ mesophases from disordered (b, f) to short-range worm-like (c, g) to long-range hexagonal (d, h) to *fcc* cubic mesophase (e, i). All scale bars are 100 nm. (j) Summary of the mesophase/surfactant concentration relationship in the monomicelle hydrogel system (PEO-*b*-PPO-*b*-PEO plus titania primitives derived from tetrabutyl titanate). (k) The representative FESEM image of the membrane morphology obtained in a high monomicelle concentration.

membranes with precise control. The mesoporous crystalline TiO$_2$ membranes, with controlled regularity, mesophase, and porosity, were finally produced after calcination in nitrogen to remove the template.

Accurate Mesostructural Control

The large-scale field-emission scanning electron microscopy (FESEM) image shows a uniform and continuous membrane structure comprised of ordered cylindrical bundles for the as-made mesostructured TiO$_2$ membrane (Figure S3). After calcination at 400 °C, a uniform and continuous mesoporous crystalline TiO$_2$ membrane with a thickness of around 640 nm can be formed (Figure 1b,c). The highly ordered mesoporous skeleton with a mean mesopore size at approximately 8 nm can be observed along different the [110] and [001] facets (Figure 1d, Figure S4). Furthermore, a similar assembly process was carried out on Ti foils (1.5 cm in diameter, Figure 1e) for further small-angle X-ray scattering (SAXS) analysis. As shown in Figure 1f, the five clear and sharp scattering peaks of both as-synthesized and calcined mesoporous TiO$_2$ membranes on the Ti foil can be indexed to the 100, 110, 200, 221, and 300 reflections, revealing the formation of the highly ordered 2D hexagonal mesophase (space group *p6mm*). Based on the nitrogen-sorption measurements, both the typical type IV isotherms with a hysteresis loop at $P/P_0 = 0.4−0.8$ and the centered pore size distribution at 7.9 nm indicate the well-defined mesoporosity (Figure 1g,h). The high-resolution transmission electron microscopy (TEM) image further visualizes the clear mesopores and ultrafine crystalline TiO$_2$ grains at around 3.2 nm (Figure 1i). The *d*-spacing of 3.5 Å can be assigned to the (101) plane of the anatase phase, consistent with the characteristic X-ray diffraction (XRD) pattern and Raman spectrum (Figure S5). Besides, the selected-area

electron diffraction (SAED) pattern recorded on the mesopore channels displays well-resolved diffraction rings, indicative of a polycrystalline anatase nature of the TiO$_2$ frameworks (Figure 1j).

It is noteworthy that this stepwise monomicelle assembly strategy provides the opportunity to precisely regulate the mesophase of crystalline TiO$_2$ membranes. A series of ordered mesoporous TiO$_2$ membranes with varied mesophases can be obtained through finely tuning the intermediate monomicelle concentration (Figure 2a), demonstrating the improved operability of such a method. Representative SEM and TEM images of the as-made mesostructured TiO$_2$ and mesoporous TiO$_2$ membranes after the calcination clearly visualize a gradual transition from disordered to worm-like (short-range ordered) to hexagonal (*p6mm*) to cubic (*Im$\bar{3}$m*) structures with the increase of the monomicelle concentration from 0.005 to 0.15 g mL^{-1} (calculated based on the amphiphilic Pluronic F127 template) (Figure 2b−i, Figure S6). In order to collect more systematical information, we carried out the same assembly processes with the monomicelle concentrations across 2 orders of magnitude (from 0.003 to 0.3 g mL^{-1}), which produced more elaborate mesophase regions at 0.003−0.005 g mL^{-1} (disordered), 0.006−0.015 g mL^{-1} (worm-like), 0.02−0.10 g mL^{-1} (2D hexagonal), and 0.15−0.25 g mL^{-1} (3D cubic) (Figure 2j, Figure S7). Concentrations higher than 0.25 g mL^{-1} turn to insoluble, suggesting that such a monomicelle system reaches the limit. Besides, when conducted at a higher temperature (80 °C), massive undesired radially oriented mesoporous TiO$_2$ spheres are generated on the membrane surface due to the water/*n*-butanol biphase in this monomicelle system[38,39] (Figure 2k, Figure S8). This response suggests that a moderate assembly condition for sufficient evaporation time is necessary to maintain a uniform
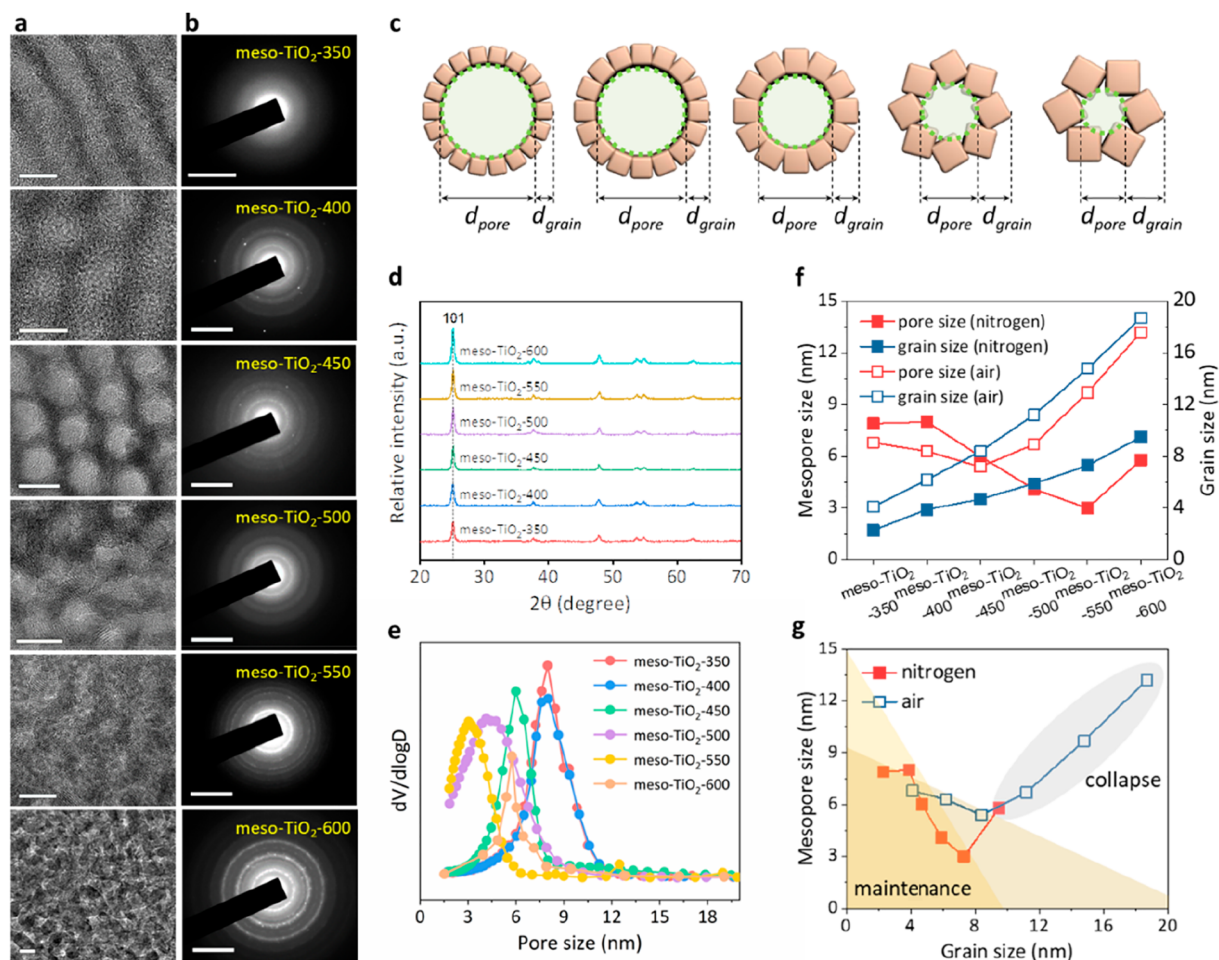
Figure 3. Balance of mesoporosity and crystallinity. (a, b) HRTEM images and corresponding SAED patterns of the mesoporous TiO_2 membranes after calcination at varied temperature in a nitrogen atmosphere. The scale bars in **a** and **b** are 10 nm and 5 1/nm, respectively. (**c**) Planar structural illustrations of the retained mesoporous TiO_2 frameworks with the shrinkage of mesoporous scaffolds and growth of TiO_2 grains. d_{pore} and d_{grain} represent the mesopore size and grain size, respectively. (**d, e**) WAXRD patterns and pore size distribution curves of the mesoporous TiO_2 samples calcined in nitrogen at different temperatures from 350 to 600 °C. (**f**) Summarized structural relationship of the mesoporous TiO_2 membranes at different temperatures, including mesopore sizes and TiO_2 grain sizes. (**g**) The mesopore size as a function of the grain size of the mesoporous TiO_2 membranes.

and continuous membrane structure instead of emulsion byproducts.

Balance of Mesoporosity and Crystallinity

The structural parameters of the mesoporous TiO_2 membranes including mesopore size and grain size can be adjusted in a certain range. By controlling the calcination process, the relationship between mesoporosity and grain size was systematically investigated. TEM images confirm the well-ordered hexagonal arrangement of TiO_2 mesopores when calcined in an inert atmosphere below 550 °C (Figure 3a). Heating treatment under nitrogen converted these as-made hybrids into mesoporous composites of TiO_2 and minor carbon; meanwhile, the more intensive diffraction rings at a higher temperature indicate the higher crystallinity (Figure 3b,c). In contrast, the carbon residues are removed after calcined under air to only 400 °C, generating pure mesoporous TiO_2 membranes (Figure S9). Note that the estimated pore size of the mesoporous TiO_2 calcined in nitrogen is larger than that in air at the same temperatures, revealing that the carbon residue from the Pluronic F127 template prevents severe contraction

of mesoporous scaffolds during the removal of organics in nitrogen.

To give more credible comparisons, samples calcined at varied temperatures in nitrogen/air (denoted as meso-TiO_2-X; X is the calcination temperature) have been collected (Table S2). As shown in Figure 3d and Figure S10, the anatase phase is constantly preserved in nitrogen, whereas the phase transition to rutile starts at 600 °C, implying the prevention of the carbon support from having access to oxygen.[40,41] The crystallite sizes calculated based on the Scherrer equation also show smaller grain sizes and a much alleviated growth trend under nitrogen, further validating the impact of protective carbon. From nitrogen sorption experiments (Figure 3e, Figures S11 and S12), with the increase of calcination temperature in nitrogen, the decline of adsorption volumes, surface areas, as well as mesopore sizes from 7.9 to 3.0 nm can be observed. However, samples treated in air are destructed when the temperature reaches 500 °C, as confirmed by the disordered TEM images (Figure S10b−f). This response indicates that accumulated nanocrystals constitute these TiO_2 mesopores, not templated from ordered composite micelles.
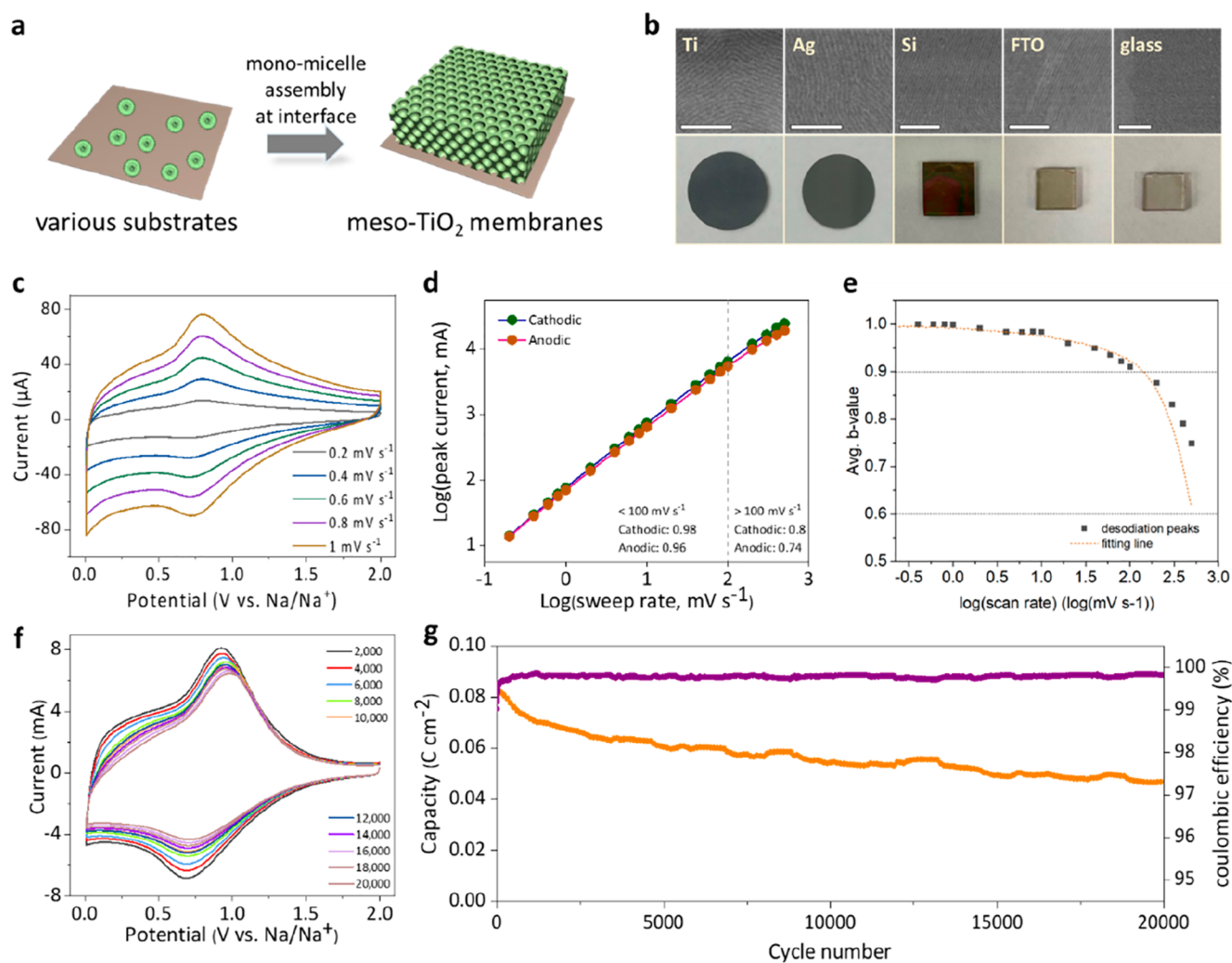
Figure 4. Flexible membrane engineering for pseudocapacitive energy storage. (**a**) Scheme for the fabrication of mesoporous TiO$_2$ membranes on various substrates. (**b**) SEM images and correlated photographic images of synthesized mesoporous TiO$_2$ membranes calcined under nitrogen on Ti, Ag, Si, FTO, and glass substrates, respectively. The scale bars in **b** are 200 nm. (**c**) CV curves at various scan rates from 0.2 to 1 mV s^{-1}. (**d**) Analysis of the *b*-value using the relationship between peak currents and scan rates. (**e**) The corresponding derivative plots of the *b*-value as a function of scan rates. (**f**) CV curves after different cycles at a scan rate of 100 mV s^{-1}. (**g**) Cycling stability of the mesoporous TiO$_2$ membrane after 20,000 cycles at a scan rate of 100 mV s^{-1}.

In brief, the summarized variations of pore size and grain size in this scenario clearly show that high temperatures undoubtedly lead to decreased mesopore size and increased pore walls, and ultimately cause structural collapse at 500 °C in air and 600 °C in nitrogen (Figure 3f). The increase of pore size behind should be attributed to piled pores comprised of gradually enlarged TiO$_2$ grains that are outside the balance for a well-defined ordered mesostructure. In the plotted grain size/ pore size curves, it can be further concluded that a proper d_{pore}/d_{grain} ratio (>2.3) is obligatory for constructing well-defined pure crystalline mesoporous structures, while ratios larger than 0.70 are sufficient for amorphous carbon integrated hybrids (Figure 3g). Such precise mesostructural control establishes a foundation on how to balance mesoporosity and crystallinity for designing optimal crystalline mesoporous materials.

Flexible Membrane Engineering for Sodium Storage

Owing to the simplicity of such a solution-processed approach, we also fabricated a series of ordered mesostructured TiO$_2$ membranes with well-crystallized frameworks by replacing the basal glass with other substrates which can endure acid and high temperature (Figure 4a). Accordingly, as visualized by SEM images (Figure 4b), substrates including Ti, Ag, Si, and FTO are allowed for the growth of ordered mesoporous crystalline TiO$_2$ membranes. Mesoscale membranes with tailored thickness from 280 nm to 1.2 μm can be achieved by simply varying the content of the monomicelle dispersion (Figure S13), demonstrating the good flexibility. Unfortunately, calcination under nitrogen to preserve carbon residual is required to maintain a smooth, cracking-free, and continuous membrane morphology with uniform thickness, possibly due to the weak affinity to substrate of pure crystalline TiO$_2$, and this shortage needs to be further investigated.

Uniform mesostructured crystalline TiO$_2$ thin membranes are desired for electrochemical applications where fast diffusion and access are important.[42,43] To this end, the ordered mesoporous crystalline TiO$_2$ membranes were *in situ* synthesized on a Ti plate without extra additives as a sodium storage electrode, possessing a continuous mesoporous membrane structure with a thickness of around 1.0 μm

(Figure S14). To probe the charge transport kinetics, cyclic voltammetry (CV) curves were first conducted at varied scan rates (Figure 4c, Figure S15). Note that the blank Ti substrate is not electrochemically active (Figure S16). When raising the scan rates, similar broad peaks with increased currents are observed. The absent peak shift suggests the fast kinetics in ion transport at both low and high scan rates. Interestingly, from the relationship between current (i) and scan rate (v), the b-values for cathodic and anodic peaks are calculated to be 0.98 and 0.96 even below 100 mV s^{-1} and the b-values also remain relatively high at greater scan rates, demonstrating the ultrafast kinetics from pseudocapacitance (Figure 4d). The derivative of the log(i)−log(v) plots show the rate-dependent b-value along with increasing sweep rates (Figure 4e), which is well-fitted through a series model proposed by Stefik and co-workers.[44−46] The surface-limited threshold (SLT) of b-value > 0.9 and the diffusion-limited threshold (DLT) of b-value < 0.6 are applied to evaluate the reaction kinetics. The mesoporous TiO$_2$ membranes have a SLT of 100 mV s^{-1}, corresponding to a (dis)charging time of 20 s, demonstrating the ultrafast kinetics from pseudocapacitance. We also performed cycling stability experiments at 100 mV s^{-1}, showing a good capacity retention (65%) after 20,000 cycles except for a slow capacity fading in initial 10 cycles (Figure 4f,g). The Coulombic efficiency is retained at over 99% for each cycle, suggesting the superior reversibility. Such facile and highly controlled mesoscopic membranes provide a foundation to design high-performance capacitive charge storage devices compared to other TiO$_2$-based anodes (Table S3).

DISCUSSION

Generally, almost all of the fabrication methods for mesostructured membranes can be classified in the well-known solvent evaporation-induced self-assembly (EISA) route or derivatives, during which the following critical steps occur: (1) interaction of amphiphilic surfactant templates and inorganic precursor sources, (2) formation of spherical micelles on the solvent interface, (3) assembly of inorganic−organic composite micelles, (4) template removal. Such a fabrication process is very mature for controlled growth of amorphous mesoporous silica due to the well-matched slow paces of hydrolysis and assembly. However, in terms of the highly reactive titanium precursors, a very dilute precursor solution and less assembly time are required to guarantee the relatively moderate hydrolysis and condensation, leading to a narrow condition for micellar assembly. For example, most of the fabricated mesoporous membranes are very thin (less than 250 nm), and the growth of mesoscopic TiO$_2$ membranes in a highly controllable manner has not been explicitly demonstrated either. On the other hand, self-assembled mesoscale TiO$_2$ membranes tend to collapse and crack inevitably, and even peel off during high-temperature crystallization because of their low thermal stability and affinity; continuous TiO$_2$ membranes with well-crystalline frameworks also await to be addressed.

Interestingly, in this work, we found a "monomicelle" primitive through a double-solvent selective evaporation strategy[38,39,47,48] and that the above issue can be finely tackled by using a stepwise monomicelle assembly approach. At first, a water-rich hydrogel that involves a stably retained F127/TiO$_2$ monomicelle subunit is obtained after the preferential THF evaporation of acidic THF/H$_2$O precursor solution at 45 °C. During this step, the fast hydrolysis of TBOT can be finely retarded because of the employment of acetic acid as a chelating agent as well as the moderate evaporation process that allows the formation of ultrafine TiO$_2$ oligomers instead of unfavored large aggregates. In the meantime, the formed monomicelle subunits after exceeding the critical micelle concentration (CMC) are dissociated due to the presence of water solvent in the system after evaporation. Hence, the intermediate hydrogel preformation of the monomicelle and TiO$_2$ oligomers allows for great manipulation in the subsequent assembly since the excessive TiO$_2$−TiO$_2$ aggregation and mismatched TiO$_2$−micelle interaction are appropriately tackled (Figure S17). As a result, in the second-step EISA process of the monomicelle dispersions, more flexible reactive conditions, such as broader concentration and evaporation time are allowed, which enabled production of the ordered mesostructured TiO$_2$ membranes with precise control. Namely, the key point of such a stepwise strategy relies on the intermediate F127/TiO$_2$ oligomer monomicelles that afford control of the mismatched precursor hydrolysis and micellar assembly separately. The mesoporous crystalline TiO$_2$ membranes, with uniform thickness and controlled mesophase and porosity, can be finally produced after calcination in nitrogen by retaining carbon as a framework support and a binder to the substrate.

It has already been recognized that the collapse issue of mesoporous frameworks occurs inevitably for crystalline mesostructures since a high enough temperature for conversion to the crystalline state easily leads to an ultralarge nanocrystal size which is incapable of building a mesopore;[13,16,49,50] however, the insight relationship has rarely been explored. In this regard, the compatibility of the mesostructural parameters and grain size by using these mesoporous TiO$_2$ membranes as a model were systematically investigated. In the first place, high temperature undoubtedly leads to decreased porosity and increased crystallinity. In this model, the ultimate structural collapse, which means the absence of ordered mesoporosity, occurs at 500 °C in air and 600 °C in nitrogen (Figure 3f). In order to achieve well-defined mesoporosity of crystalline frameworks rather than piled mesopores of enlarged TiO$_2$ grains, a size principle between mesopores and grains is indispensable. For the pure mesoporous TiO$_2$ structures, the value of d_{pore}/d_{grain} has to be larger than 2.3 (Figure 3g, Figure S18). Namely, a well-preserved pore size constructed by nanocrystals at ~1 nm is certainly bigger than 2.3 nm; otherwise, the templated mesopore is destroyed or comprised of disordered accumulations. For the mesoporous TiO$_2$−C composites, this value is tolerable (>0.7) because the amorphous carbon is able to perform as a deformable filler to retain such rigid TiO$_2$ frameworks. Such a mesostructural relationship establishes a foundation on how to balance mesoporosity and crystallinity for designing optimal crystalline mesoporous materials.

The excellent pseudocapacitive charge storage behavior is attributed to the textual properties of the ordered mesoporous TiO$_2$ membranes with a crystalline skeleton. The ordered and large mesoporosity afford comprehensive utilization of electrochemically active TiO$_2$, which significantly favors the rapid faradaic redox reaction between Na$^+$ and TiO$_2$.[51−53] The tiny and tunable TiO$_2$ grains in mesoporous frameworks afford a short diffusion distance and determine the near-surface Na$^+$ intercalation feature, thus leading to almost overall capacitive reactions.[54] The carbon network as an effective conductive agent also facilitates electron transport. These factors are

possibly responsible for the ultrafast pseudocapacitive sodiation, which could have profound implications for high-power applications, fast-charging devices, and high-performance mesoporous devices such as diffusion-involved catalysis and sensing.

CONCLUSIONS

Together, we have demonstrated a stepwise monomicelle assembly strategy for the facile growth of highly ordered mesoporous TiO_2 membranes with well-crystalline anatase pore walls, uniform thickness (around 0.28−2 μm) at high repeatability, flexibility, and extendibility. The salient aspect in this protocol is to separately control the fast hydrolysis of the reactive titanium source and moderate assembly of mono-micelle units, thus providing adequate opportunity to guarantee the high mesoscale regularity, good crystallized mesopore walls, tunable mesophase, and continuous membrane integrality. For balancing the mesoporosity and crystallinity, proper d_{pore}/d_{grain} ratios of 2.3 and 0.7 are obligatory for pure crystalline mesostructures and carbon-integrated hybrids, respectively. Due to the high surface area and desirable porosity, the electrode composed of pure active mesoporous TiO_2 membranes can realize ultrafast charge transport kinetics and excellent cyclability (65% retention over 20,000 cycles). The versatile and flexible manipulation of the presented mesoscopic TiO_2 architecture can be exploited in a new generation of practical mesoporous devices such as electrochemical storage, solar cells, and diffusion associated catalysis.

ASSOCIATED CONTENT

ⓢ Supporting Information

The Supporting Information is available free of charge at https://pubs.acs.org/doi/10.1021/jacsau.3c00007.

> Additional experimental details for the preparations, characterizations of materials, and electrochemical measurements (Figures S1−S17 and Tables S1−S3) (PDF)

AUTHOR INFORMATION

Corresponding Authors

Dongyuan Zhao − *College of Energy Materials and Chemistry, College of Chemistry and Chemical Engineering, Inner Mongolia University, Hohhot 010070, P. R. China; Laboratory of Advanced Materials, Department of Chemistry, College of Chemistry and Materials, Fudan University, Shanghai 200433, P. R. China;* ⓘ orcid.org/0000-0001-8440-6902; Email: dyzhao@fudan.edu.cn

Qiulong Wei − *Department of Materials Science and Engineering, College of Materials, Xiamen University, Xiamen 361005, P. R. China;* ⓘ orcid.org/0000-0002-9551-8309; Email: qlwei@xmu.edu.cn

Kun Lan − *College of Energy Materials and Chemistry, College of Chemistry and Chemical Engineering, Inner Mongolia University, Hohhot 010070, P. R. China; Laboratory of Advanced Materials, Department of Chemistry, College of Chemistry and Materials, Fudan University, Shanghai 200433, P. R. China;* ⓘ orcid.org/0000-0001-8983-0155; Email: k_lan@imu.edu.cn

Authors

Lu Liu − *Laboratory of Advanced Materials, Department of Chemistry, College of Chemistry and Materials, Fudan University, Shanghai 200433, P. R. China*

Jiayu Yu − *Department of Materials Science and Engineering, College of Materials, Xiamen University, Xiamen 361005, P. R. China*

Yuzhu Ma − *College of Energy Materials and Chemistry, College of Chemistry and Chemical Engineering, Inner Mongolia University, Hohhot 010070, P. R. China; Laboratory of Advanced Materials, Department of Chemistry, College of Chemistry and Materials, Fudan University, Shanghai 200433, P. R. China*

Jun-Ye Zhang − *Laboratory of Advanced Materials, Department of Chemistry, College of Chemistry and Materials, Fudan University, Shanghai 200433, P. R. China*

Zirui Lv − *Laboratory of Advanced Materials, Department of Chemistry, College of Chemistry and Materials, Fudan University, Shanghai 200433, P. R. China*

Sixing Yin − *Laboratory of Advanced Materials, Department of Chemistry, College of Chemistry and Materials, Fudan University, Shanghai 200433, P. R. China*

Complete contact information is available at:
https://pubs.acs.org/10.1021/jacsau.3c00007

Notes

The authors declare no competing financial interest.

ACKNOWLEDGMENTS

REFERENCES

(1) Jiang, Z.; Xu, X.; Ma, Y.; Cho, H. S.; Ding, D.; Wang, C.; Wu, J.; Oleynikov, P.; Jia, M.; Cheng, J.; Zhou, Y.; Terasaki, O.; Peng, Y.; Zan, L.; Deng, H. Filling metal–organic framework mesopores with TiO_2 for CO_2 photoreduction. *Nature* **2020**, *586*, 549−554.

(2) Hanikel, N.; Prevot, M. S.; Yaghi, O. M. MOF water harversters. *Nat. Nano.* **2020**, *15*, 348−355.

(3) Moreno, C.; Vilas-Varela, M.; Kretz, B.; Garcia-Lekue, A.; Costache, M. V.; Paradinas, M.; Panighel, M.; Ceballos, G.; Valenzuela, S. O.; Pena, D.; Mugarza, A. Bottom-up synthesis of multifunctional nanoporous graphene. *Science* **2018**, *360*, 199−203.

(4) Ling, T.; Da, P.; Zheng, X.; Ge, G.; Hu, Z.; Wu, M.; Du, X.; Hu, W.; Jaroniec, M.; Qiao, S. Atomic-level structure engineering of metal oxides for high-rate oxygen intercalation pseudocapacitance. *Sci. Adv.* **2018**, *4*, No. eaau6261.

(5) Yu, L.; Hu, H.; Wu, H.; Lou, X. Complex hollow nanostructures: synthesis and energy-related applications. *Adv. Mater.* **2017**, *29*, 1604563.

(6) Li, Z. L.; Li, Z. Q.; Zuo, C.; Fang, X. Nanostructured TiO_2 applications in UV photodetectors: a review. *Adv. Mater.* **2022**, *34*, 2109083.

(7) Antonelli, D. M.; Ying, J. Y. Synthesis of hexagonally packed mesoporous TiO2 by a modified sol-gel method. *Angew. Chem., Int. Ed.* **1995**, *34*, 2014−2017.

(8) Warren, S. C.; Messina, L. C.; Slaughter, L. S.; Kamperman, M.; Zhou, Q.; Gruner, S. M.; DiSalvo, F. J.; Wiesner, U. Ordered mesoporous materials from metal nanoparticle-block copolymer self-assembly. *Science* **2008**, *320*, 1748−1752.

(9) Jiang, B.; Li, C.; Dag, O.; Abe, H.; Takei, T.; Imai, T.; Hossain, M. S. A.; Islam, M. T.; Wood, K.; Henzie, J.; Yamauchi, Y. Mesoporous metallic rhodium nanoparticles. *Nat. Commun.* **2017**, *8*, 15581.

(10) Jiang, B.; Guo, Y.; Kim, J.; Whitten, A. E.; Wood, K.; Kani, K.; Rowan, A. E.; Henzie, J.; Yamauchi, Y. Mesoporous metallic iridium nanosheets. *J. Am. Chem. Soc.* **2018**, *140*, 12434−12441.

(11) Lim, H.; Kani, K.; Henzie, J.; Nagaura, T.; Nagraha, A. S.; Iqbal, M.; Ok, Y. S.; Hossain, M. S. A.; Bando, Y.; Wu, K. C.; Kim, H.; Rowan, A. E.; Na, J.; Yamauchi, Y. A universal approach for the synthesis of mesoporous gold, palladium and platinum films for applications in electrocatalysis. *Nat. Protoc.* **2020**, *15*, 2980−3008.

(12) Guan, B.; Yu, L.; Li, J.; Lou, X. A universal cooperative assembly-directed method for coating of mesoporous TiO₂ nanoshells with enhanced lithium storage properties. *Sci. Adv.* **2016**, *2*, No. e1501554.

(13) Lee, J.; Orilall, C. M.; Warren, S. C.; Kamperman, M.; DiSalvo, F. J.; Wiesner, U. Direct access to thermally stable and highly crystalline mesoporous transition-metal oxides with uniform pores. *Nat. Mater.* **2008**, *7*, 222−228.

(14) Robbins, S. W.; Beaucage, P. A.; Sai, H.; Tan, K. W.; Werner, J. G.; Sethna, J. P.; DiSalvo, F. J.; Gruner, S. M.; Dover, R. B. V.; Wiesner, U. Block copolymer self-assembly-directed synthesis of mesoporous gyroidal superconductors. *Sci. Adv.* **2016**, *2*, No. e1501119.

(15) Tian, B.; Liu, X.; Tu, B.; Yu, C.; Fan, J.; Wang, L.; Xie, S.; Stucky, G. D.; Zhao, D. Y. Self-adjusted synthesis of ordered stable mesoporous minerals by acid-base pairs. *Nat. Mater.* **2003**, *2*, 159−163.

(16) Li, D.; Zhou, H.; Honma, I. Design and synthesis of self-ordered mesoporous nanocomposite through controlled in-situ crystallization. *Nat. Mater.* **2004**, *3*, 65−72.

(17) Lv, H.; Xu, D.; Sun, L.; Henzie, J.; Lopes, A.; Gu, Q.; Yamauchi, Y.; Liu, B. Asymmetric multimetallic mesoporous nanospheres. *Nano Lett.* **2019**, *19*, 3379−3385.

(18) Kang, Y.; Guo, Y.; Zhao, J.; Jiang, B.; Guo, J.; Tang, Y.; Li, H.; Malgras, V.; Amin, M. A.; Nara, H.; Sugahara, Y.; Yamauchi, Y.; Asahi, T. Soft template-based synthesis of mesoporous phosphorus- and boron-codoped NiFe-based alloys for efficient oxygen evolution reaction. *Small.* **2022**, *18*, 2203411.

(19) Kang, Y.; Tang, Y.; Zhu, L.; Jiang, B.; Xu, X.; Guselnikova, O.; Li, H.; Asahi, T.; Yamauchi, Y. Porous nanoarchitectures of nonprecious metal borides: from controlled synthesis to heterogeneous catalyst applications. *ACS Catal.* **2022**, *12*, 14773−14793.

(20) Qiu, P.; Ma, B.; Hung, C.; Li, W.; Zhao, D. Y. Spherical mesoporous materials from single to multilevel architectures. *Acc. Chem. Res.* **2019**, *52*, 2928−2938.

(21) Choi, S. Y.; Mamak, M.; Coombs, N.; Chopra, N.; Ozin, G. A. Thermally stable two-dimensional hexagonal mesoporous nanocrystalline anatase, meso-nc-TiO₂: bulk and crack-free thin film morphologies. *Adv. Funct. Mater.* **2004**, *14*, 335−344.

(22) Guldin, S.; Docampo, P.; Stefik, M.; Kamita, G.; Wiesner, U.; Snaith, H.; Steiner, U. Layer-by-layer formation of block-copolymer-derived TiO₂ for solid-state dye-sensitized solar cells. *Small* **2012**, *8*, 432−440.

(23) Brezesinski, T.; Wang, J.; Polleux, J.; Dunn, B.; Tolbert, S. Templated nanocrystal-based porous TiO₂ films for next-generation electrochemical capacitors. *J. Am. Chem. Soc.* **2009**, *131*, 1802−1809.

(24) Zhang, H.; Banfield, J. F. Structural characteristics and mechanical and thermodynamic properties of nanocrystalline TiO₂. *Chem. Rev.* **2014**, *114*, 9613−9644.

(25) Li, W.; Wu, Z.; Wang, J.; Elzatahry, A.; Zhao, D. Y. A perspective on mesoporous TiO₂ materials. *Chem. Mater.* **2014**, *26*, 287−298.

(26) Cölfen, H.; Antonietti, M. Mesocrystals: inorganic superstructures made by highly parallel crystallization and controlled alignment. *Angew. Chem., Int. Ed.* **2005**, *44*, 5576−5591.

(27) Yang, P.; Zhao, D.; Margolese, D. I.; Chmelka, B. F.; Stucky, G. D. Generalized syntheses of large-pore mesoporous metal oxides with semicrystalline frameworks. *Nature* **1998**, *396*, 152−155.

(28) Luo, W.; Li, Y.; Dong, J.; Wei, J.; Xu, J.; Deng, Y.; Zhao, D. Y. A resol-assisted co-assembly approach to crystalline mesoporous niobia spheres for electrochemical biosensing. *Angew. Chem., Int. Ed.* **2013**, *52*, 10505−10510.

(29) Zhang, J.; Deng, Y.; Gu, D.; Wang, S.; She, L.; Che, R.; Wang, Z.; Tu, B.; Xie, S.; Zhao, D. Y. Ligand-assisted assembly approach to synthesize large-pore ordered mesoporous titania with thermally stable and crystalline framework. *Adv. Energy Mater.* **2011**, *1*, 241−248.

(30) Feng, D.; Luo, W.; Zhang, J.; Xu, M.; Zhang, R.; Wu, H.; Lv, Y.; Asiri, A. M.; Khan, S. B.; Rahman, M. M.; Zheng, G.; Zhao, D. Y. Mulit-layered mesoporous TiO₂ films with large pores and highly crystalline frameworks for efficient photoelectrochemical conversion. *J. Mater. Chem. A* **2013**, *1*, 1591−1599.

(31) Brinker, C. J.; Lu, Y.; Sellinger, A.; Fan, H. Evaporation-induced self-assembly: nanostructures made easy. *Adv. Mater.* **1999**, *11*, 579−585.

(32) Shi, Y.; Wan, Y.; Liu, R.; Tu, B.; Zhao, D. Y. Synthesis of highly ordered mesoporous crystalline WS₂ and MoS₂ via a high-temperature reductive sulfuration route. *J. Am. Chem. Soc.* **2007**, *129*, 9522−9531.

(33) Liu, Y.; Lan, K.; Li, S.; Liu, Y.; Kong, B.; Wang, G.; Zhang, P.; Wang, R.; He, H.; Ling, Y.; Al-Enizi, A. M.; Elzatahry, A. A.; Cao, Y.; Chen, G.; Zhao, D. Y. Constructing three-dimensional mesoporous bouquet-posy-like TiO₂ superstructures with radially oriented mesochannels and single-crystal walls. *J. Am. Chem. Soc.* **2017**, *139*, 517−526.

(34) Jiao, F.; Hill, A. H.; Harrison, A.; Berko, A.; Chadwick, A. V.; Bruce, P. G. Synthesis of ordered mesoporous NiO with crystalline walls and a bimodal pore size distribution. *J. Am. Chem. Soc.* **2008**, *130*, 5262−5266.

(35) Wu, C.; Ohsuna, T.; Kuwabara, M.; Kuroda, K. Formation of highly ordered mesoporous titania films consisting of crystalline nanopillars with inverse mesospace by structural transformation. *J. Am. Chem. Soc.* **2006**, *128*, 4544−4545.

(36) Shan, F.; Lu, X.; Zhang, Q.; Wu, J.; Wang, Y.; Bian, F.; Lu, Q.; Fei, Z.; Dyson, P. J. A facile approach for controlling the orientation of one-dimensional mesochannels in mesoporous titania films. *J. Am. Chem. Soc.* **2012**, *134*, 20238−20241.

(37) Malgras, V.; Shirai, Y.; Takei, T.; Yamauchi, Y. Coalescence-driven verticality in mesoporous TiO₂ thin films with long-range ordering. *J. Am. Chem. Soc.* **2020**, *142*, 15815−15822.

(38) Lan, K.; Wang, R.; Zhang, W.; Zhao, Z.; Elzatahry, A.; Zhang, X.; Liu, Y.; Al-Dhayan, D.; Xia, Y.; Zhao, D. Y. Mesoporous TiO₂ microspheres with precisely controlled crystallites and architectures. *Chem.* **2018**, *4*, 2436−2450.

(39) Lan, K.; Liu, L.; Zhang, J.; Wang, R.; Zu, L.; Lv, Z.; Wei, Q.; Zhao, D. Y. Precisely designed mesoscopic titania for high-volumetric-density pseudocapacitance. *J. Am. Chem. Soc.* **2021**, *143*, 14097−14105.

(40) Li, Y.; Luo, W.; Qin, N.; Dong, J.; Wei, J.; Li, W.; Feng, S.; Chen, J.; Xu, J.; Elzatahry, A.; Es-Saheb, M.; Deng, Y.; Zhao, D. Y. Highly ordered mesoporous tungsten oxides with a large pore size and crystalline framework for H₂S sensing. *Angew. Chem., Int. Ed.* **2014**, *53*, 9035−9040.

(41) Liu, L.; Yang, X.; Xie, Y.; Liu, H.; Zhou, X.; Xiao, X.; Ren, Y.; Ma, Z.; Cheng, X.; Deng, Y.; Zhao, D. Y. A universal lab-on-salt-particle approach to 2D single-layer ordered mesoporous materials. *Adv. Mater.* **2020**, *32*, 1906653.

(42) Wu, X.; Zhang, H.; Zhang, J.; Lou, X. Recent advances on transition metal dichalcogenides for electrochemical energy conversion. *Adv. Mater.* **2021**, *33*, 2008376.

(43) Chao, D.; Zhou, W.; Xie, F.; Ye, C.; Li, H.; Jaroniec, M.; Qiao, S. Roadmap for advanced aqueous batteries: from design of materials to applications. *Sci. Adv.* **2020**, *6*, No. eaba4098.

(44) van den Bergh, W.; Stefik, M. Understanding Rapid Intercalation Materials One Parameter at a Time. *Adv. Funct. Mater.* **2022**, *32*, 2204126.

(45) Bergh, W.; Lokupitiya, H. N.; Vest, N. A.; Reid, B.; Guldin, S.; Stefik, M. Nanostructure Dependence of T-Nb_2O_5 Intercalation Pseudocapacitance Probed Using Tunable Isomorphic Architectures. *Adv. Funct. Mater.* **2021**, *31*, 2007826.

(46) van den Bergh, W.; Larison, T.; Jesus Jara Fornerod, M.; Guldin, S.; Stefik, M. Faster intercalation pseudocapacitance enabled by adjustable amorphous titania where tunable isomorphic architectures reveal accelerated lithium diffusivity. *Batteries & Supercapas* **2022**, *5*, No. e202200122.

(47) Lan, K.; Xia, Y.; Wang, R.; Zhao, Z.; Zhang, W.; Zhang, X.; Elzatahry, A.; Zhao, D. Y. Confined interfacial mono-micelle assembly for precisely controlled coating single-layered titania mesopores. *Matter* **2019**, *1*, 527−538.

(48) Liu, Y.; Che, R.; Fan, J.; Sun, Z.; Wu, Z.; Wang, M.; Li, B.; Wei, J.; Wei, Y.; Wang, G.; Guan, G.; Elzatahry, A.; Bagabas, A.; Al-Enizi, A.; Deng, Y.; Peng, H.; Zhao, D. Y. Radially oriented mesoporous TiO_2 microspheres with single-crystal-like anatase walls for high-efficiency optoelectronic devices. *Sci. Adv.* **2015**, *1*, No. e1500166.

(49) Warren, S. C.; Messina, L. C.; Slaughter, L. S.; Kamperman, M.; Zhou, Q.; Gruner, S. M.; DiSalvo, F. J.; Wiesner, U. Ordered mesoporous materials from metal nanoparticle-block copolymer self-assembly. *Science* **2008**, *320*, 1748−1752.

(50) Malgras, V.; Ataee-Esfahani, H.; Wang, H.; Jiang, B.; Li, C.; Wu, K.; Kim, J. H.; Yamauchi, Y. Nanoarchitectures for mesoporous metals. *Adv. Mater.* **2016**, *28*, 993−1010.

(51) Zhang, G.; Wu, H.; Song, T.; Paik, U.; Lou, X. TiO_2 hollow spheres composed of highly crystalline nanocrystals exhibit superior lithium storage properties. *Angew. Chem., Int. Ed.* **2014**, *53*, 12590−12593.

(52) Huang, Y.; Fang, Y.; Lu, X.; Luan, D.; Lou, X. Co_3O_4 hollow nanoparticles embedded in mesoporous walls of carbon nanoboxes for efficient lithium storage. *Angew. Chem., Int. Ed.* **2020**, *59*, 19914−19918.

(53) Jiao, Y.; Zheng, Y.; Jaroniec, M.; Qiao, S. Design of electrocatalysts for oxygen and hydrogen-involving energy conversion reactions. *Chem. Soc. Rev.* **2015**, *44*, 2060−2086.

(54) Jiang, C.; Wei, M.; Qi, Z.; Kudo, T.; Honma, I.; Zhou, H. Particle size dependence of the lithium storage capability and high rate performance of nanocrystalline TiO_2 electrode. *J. Power Sources* **2007**, *166*, 239−243.